Petroleum Science 22 (2025) 2747–2759

Contents lists available at ScienceDirect

Petroleum Science

journal homepage: www.keaipublishing.com/en/journals/petroleum-science

Original Paper

Influence of CO_2–brine–kerogen wettability on CO_2 sequestration in shale: Implications from molecular dynamics simulation

Kan-Yuan Shi [a, b, c], Jun-Qing Chen [a, d, e, *], Xiong-Qi Pang [a, b, **], Sha-Sha Hui [f], Zhang-Xin Chen [a, g, ***], Ben-Jie-Ming Liu [g], Yu-Jie Jin [a, b], Si-Jia Zhang [a, b]

[a] State Key Laboratory of Petroleum Resources and Engineering, China University of Petroleum (Beijing), Beijing, 102249, China
[b] College of Geosciences, China University of Petroleum (Beijing), Beijing, 102249, China
[c] Petroleum Exploration and Production Research Institute, SINOPEC, Beijing, 102206, China
[d] Basic Research Center for Energy Interdisciplinary, College of Science, China University of Petroleum (Beijing), Beijing, 102249, China
[e] Beijing Key Laboratory of Optical Detection Technology for Oil and Gas, College of Science, China University of Petroleum (Beijing), Beijing, 102249, China
[f] Research Institute of Petroleum Exploration and Development, PetroChina, Beijing, 100083, China
[g] Eastern Institute of Technology, Ningbo, 315200, Zhejiang, China

ARTICLE INFO

Article history:
Received 15 October 2024
Received in revised form
5 January 2025
Accepted 26 March 2025
Available online 28 March 2025

Edited by Jie Hao

Keywords:
Wettability
Kerogen
Shale
CO_2 sequestration
Molecular dynamics

ABSTRACT

As the main factor influencing the flow and preservation of underground fluids, wettability has a profound impact on CO_2 sequestration (CS). However, the influencing factors and internal interaction mechanisms of shale kerogen wettability remain unclear. In this study, we used molecular dynamics to simulate the influence of temperature, pressure, and salinity on wettability. Furthermore, the results were validated through various methods such as mean square displacement, interaction energy, electrostatic potential energy, hydrogen bonding, van der Waals forces, and electrostatic forces, thereby confirming the reliability of our findings. As temperature increases, water wettability on the surface of kerogen increases. At CO_2 pressures of 10 and 20 MPa, as the temperature increases, the kerogen wettability changes from CO_2 wetting to neutral wetting. As the CO_2 pressure increases, the water wettability on the surface of kerogen weakens. When the pressure is below 7.375 MPa and the temperature is 298 or 313 K, kerogen undergoes a wettability reversal from neutral wetting to CO_2 wetting. As salinity increases, water wettability weakens. Divalent cations (Mg^{2+} and Ca^{2+}) have a greater impact on wettability than monovalent cations (Na^{+}). Water preferentially adsorbs on N atom positions in kerogen. CO_2 is more likely to form hydrogen bonds and adsorb on the surface of kerogen than H_2O. As the temperature increases, the number of hydrogen bonds between H_2O and kerogen gradually increases, while the increase in pressure reduces the number of hydrogen bonds. Although high pressure helps to increase an amount of CS, it increases the permeability of a cap rock, which is not conducive to CS. Therefore, when determining CO_2 pressure, not only a storage amount but also the storage safety should be considered. This research method and results help optimize the design of CS technology, and have important significance for achieving sustainable development.

1. Introduction

Carbon capture and geological storage (CCGS) can reduce CO_2 emissions by injecting CO_2 into underground strata with a complete geological structure and good sealing (Kim and Makhnenko, 2023; Deng et al., 2023). CCGS is an important foundation for achieving carbon neutrality goals and plays a significant role in promoting sustainable development (Wang et al., 2023; Zhang et al., 2024). The oil and gas industry greatly benefits from the development of CCGS. There are several oil reservoirs, depleted gas

* Corresponding author.
** Corresponding author.
*** Corresponding author.
E-mail addresses: chenjq@cup.edu.cn, cjq7745@163.com (J.-Q. Chen), pangxq@cup.edu.cn (X.-Q. Pang), zhachen@ucalgary.ca (Z.-X. Chen).

https://doi.org/10.1016/j.petsci.2025.03.040

reservoirs, and deep saline layers in large and medium-sized sedimentary basins worldwide, which can be favorable locations for carbon storage (Kassa et al., 2022). CCGS can not only achieve the goal of emission reduction, but also significantly improve oil recovery (Birkholzer et al., 2015; Famoori et al., 2021; Ali et al., 2022a). Given the inherent advantages of the hydrocarbon industry, oil and gas companies are continuously increasing their research and investment in CCGS (Sun et al., 2023). Shale reservoirs are widely distributed globally. With the continuous progress of shale hydrocarbon exploration and development, global shale hydrocarbon production has rapidly increased (Hu et al., 2022, 2023, 2024; Wang et al., 2022a, 2022b; Zhang et al., 2023). Therefore, the study of CO_2 sequestration (CS) in shale is essential.

Wettability is a key parameter governing the interaction between underground fluids and shale (Yoshimitsu et al., 2002). It significantly influences capillary pressure and fluid mobility in shale, thereby facilitating the successful implementation of CS projects (Awolayo et al., 2016; Huang et al., 2024). Various methods have been employed to characterize shale wettability; however, the factors influencing wettability are very complex, and the experimental results obtained differ significantly. Previously, it was widely believed that shale reservoirs are hydrophilic (Al-Yaseri et al., 2021). However, an interaction between functional groups and their redistribution on surfaces during an interaction between underground fluids and shale can lead to a transition from water wetting to CO_2 wetting (Lu et al., 2021). In general, shale–brine–CO_2 systems often exhibit moderate to strong CO_2 wetting under high pressure, low temperature, high salinity, and high TOC content (Pan et al., 2019; Ali et al., 2023). However, different results have been reported. According to Gholami et al. (2021), as the concentration of $CaCl_2$ increases, its water wetting gradually increases. This may be related to various factors, such as different maturity, a surface area, surface roughness, and distribution of organic matter in shale (Yekeen et al., 2021), indicating that a measured contact angle (CA) varies under different influencing factors. Particularly in experiments, there are certain limitations and uncertainties in macroscopic CA measurements (Pan et al., 2020; Rego et al., 2022; Ali et al., 2024). Thus, microscopic simulation methods should be employed to study shale–brine–CO_2 wettability and compare their results with experimental results to explore the reasons for the discrepancy in reported results (Xue et al., 2015).

Recently, owing to the superiority of molecular dynamics (MD) in microscopic research, it has been widely employed to study the wettability (Hu et al., 2016). Yu et al. (2020) studied the wettability changes in graphene–brine–CO_2 systems under various influencing factors using MD. By comparing their results with previous studies, they confirmed the reliability of MD simulations. Al-Yaseri et al. (2023) studied the wettability of sandstone and carbonate rocks under different conditions through MD to identify the reasons for the differences in experimental results caused by the measured wettability. Wang and Chang (2024) investigated the wettability of graphene, quartz, kaolinite, calcite, and illite under different temperatures, pressures, and mineralization levels through MD, which deepened our understanding of the petroleum behavior in the nanopores of shale oil reservoirs. However, currently, few researchers have used real kerogen to study water wetting under CO_2 pressure.

In our previous study, because of the lack of a real kerogen model, we used graphene instead of organic matter for wettability research (Shi et al., 2022), which yielded reliable results. However, graphene still has some differences from kerogen. The influence of temperature, pressure, and salinity on the wettability of kerogen, especially microscopic CA measurements and internal interaction, is unclear. Therefore, we built a real kerogen model (Shi et al., 2024). Shale wettability is restudied using this real kerogen model. First, we study the factors influencing the wettability of organic matter in shale. Our results are then validated through various methods, such as mean square displacement (MSD), interaction energy, electrostatic potential energy, hydrogen bonding, van der Waals forces, electrostatic forces, and comparisons with previous simulation and experimental results, thereby confirming the reliability of our findings. Our findings will not only help to understand the microwettability mechanisms of shale to compensate for the shortcomings of experimental methods but also have important significance for CS.

2. Methodology

2.1. Simulation principle

MD is a method for studying the physical movement of atoms and molecules, providing detailed insights into the dynamic evolution of systems (Alder and Wainwright, 1957). The interaction potential between atoms significantly influences the accuracy of system calculation results, so the potential function is crucial in MD (Chakraborty et al., 2015). The COMPASS force field is widely used to study mineral surfaces to study atomic interactions (Sun, 1998; Chang et al., 2018; Savin and Mazo, 2020; Heydari et al., 2021):

$$E_{\text{total}} = E_{\text{valence}} + E_{\text{non-bond}} \tag{1}$$

where E_{total} denotes the total energy, kcal/mol; E_{valence} denotes the bond energy, kcal/mol; $E_{\text{non-bond}}$ denotes the nonbond energy, kcal/mol.

Nonbond energy includes gravitational and repulsive forces (Zendehboudi et al., 2018; Al-Raeei and El-Daher, 2019):

$$E_{\text{non-bond}} = E_{ij} + E_{\text{coulomb}} \tag{2}$$

$$E_{ij} = \sum_{i,j} \varepsilon_{ij} \left[2\left(\frac{r_{ij}^{o}}{r_{ij}}\right)^{9} - 3\left(\frac{r_{ij}^{o}}{r_{ij}}\right)^{6} \right] \tag{3}$$

where E_{ij} denotes the van der Waals energy, kcal/mol; E_{coulomb} denotes the electrostatic interaction energy, kcal/mol; r_{ij} denotes the distance between particles i and j, Å; ε_{ij} denotes the potential well depth, kcal/mol; r_{ij}^{o} denotes the distance between the pairs of particles with a potential of 0, Å.

2.2. Wettability model construction

All models in this study were constructed using Materials Studio software. First, we prepared individual water molecules (Fig. 1(a)), CO_2 molecules (Fig. 1(a)), and kerogen molecules (Fig. 1(a)). Then, 500 water molecules were combined to obtain the initial water model (Fig. 1(b)). We combined 4000 CO_2 molecules to obtain the initial CO_2 model (7 nm × 7 nm × 5.5 nm) (Fig. 1(b)). We combined 10 two–dimensional kerogen models to obtain the initial kerogen model (7 nm × 7 nm × 1 nm) (Fig. 1(b)). The initial water, CO_2, and kerogen models were then geometrically optimized and energy minimized to ensure that their structures were in the most stable state. Finally, the optimized models were combined using software and subjected to geometric optimization and energy minimization to obtain the final initial wettability model (7 nm × 7 nm × 14 nm) (Fig. 1(c)). When conducting the dynamics of the final wettability model, it is necessary to fix kerogen, relax the CO_2 and water molecules, and add a 5 nm vacuum layer at the top to eliminate periodic effects.

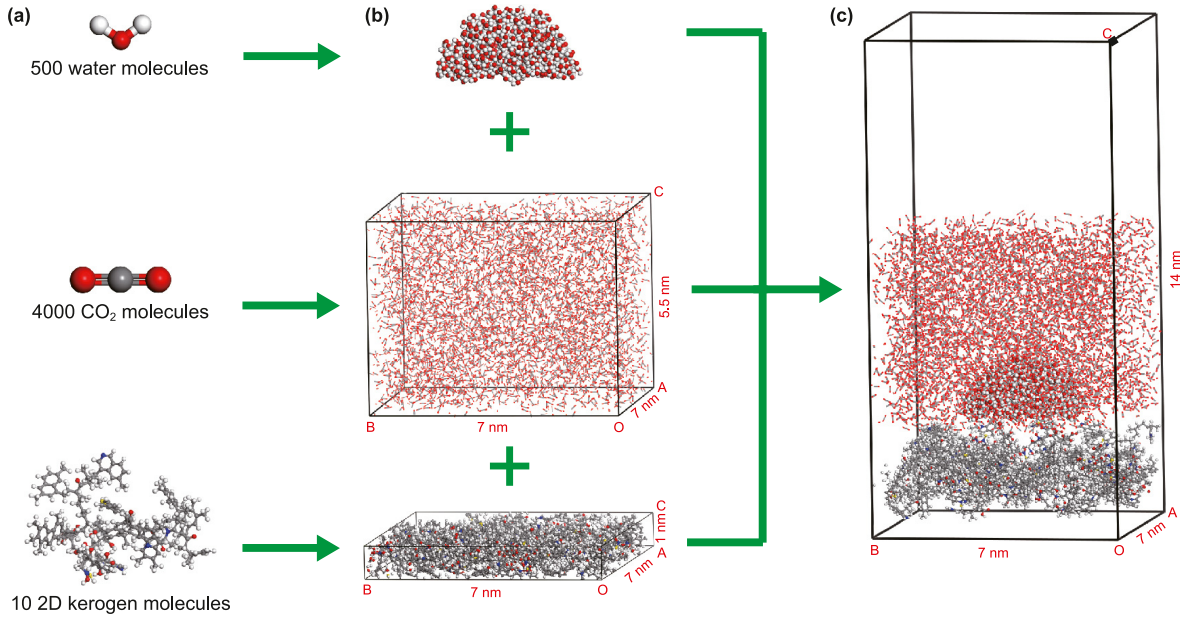

Fig. 1. The construction process of the wettability model: (**a**) individual water, CO_2, and kerogen molecules, (**b**) initial water, CO_2, and kerogen models, and (**c**) final wettability model.

The water molecule model was constructed using the Build Nanocluster module. The CO_2 and kerogen models were constructed using the Amorphous Cell module. The kerogen molecule was previously constructed by Shi et al. (2024). The molecular formula of kerogen is $C_{199}H_{240}O_{20}N_6S_2$. The shale samples for constructing kerogen molecules were taken from the Gaoshangbao area in the northeast of Nanpu Sag in Bohai Bay Basin, China, which is one of the main onshore oil-producing areas in Nanpu Sag (Fig. 2) (Chen et al., 2021). The shale sample has a depth of 4108.9 m and belongs to the third member of the Dongying Formation. R_o is 0.63%. The kerogen density is 1.106 g/cm^3.

2.3. Simulated parameters

It is necessary to perform geometric optimization on the initial model, followed by dynamic simulation. Geometric optimization can eliminate potential non–physical interactions in the structure and provide a stable foundation for subsequent MD simulations. To ensure sufficient simulation time, we set the time step for dynamic simulation to 1 fs and the system simulation time to 2000 ps (Zhu et al., 2015). In this study, the dynamic simulation time was set to 2000 ps, and the duration was chosen based on the time required for molecular behavior to reach equilibrium. We confirmed the equilibrium state of molecular behavior by analyzing the radial distribution function (RDF) and energy change curve of the system. Specifically, at the beginning of the simulation, the system energy fluctuates greatly, but in the following time, the system energy and RDF tend to stabilize, indicating that the system has reached an equilibrium state. The simulation steps and conditions are shown in Fig. 3. A cutoff distance of 12.5 Å was used in the simulation to improve computational efficiency and avoid accuracy loss caused by short cutoff distance (Zhong et al., 2013; Xia et al., 2016). In order to maintain the stable temperature state of the system, we adopted the Andersen thermostat method (Andersen, 1980), which can effectively achieve temperature control through random momentum exchange. In the calculation of electrostatic interactions, the Ewald method was used. This method can accurately handle long–range electrostatic interactions under periodic boundary conditions. The simulation conditions are detailed in Table 1.

2.4. Measurement of contact angle

Currently, several scholars have used MD to measure the microwettability of minerals (Bhattacharjee and Khan, 2019; Pham and Walsh, 2021). The geometric method is the most intuitive and commonly used method for measuring microcontact angles (Li and Wang, 2017). As shown in Fig. 4, when the surface of kerogen is hydrophilic or hydrophobic, the CA is acute or obtuse, respectively. When measuring the CA, the first step is to draw a concentration distribution map of water on the surface of kerogen and then use the isodensity curve fitting method to calculate the CA of kerogen (Fig. 4(c)) as follows:

$$(R-h)^2 + x^2 = R^2 \tag{4}$$

$$\cos\theta = 1 - \frac{h}{R} \tag{5}$$

where h denotes the distance from the highest droplet point to the mineral surface, and R denotes the radius of the sphere.

3. Results

3.1. Influence of temperature on wettability

The variation characteristics of the CA of the surface of kerogen at 298, 313, 323, and 343 K were simulated via MD. By the distribution pattern of water on the surface of kerogen at the last moment of simulation (2000 ps), which can directly reflect kerogen wettability. With an increase in temperature, the contact area between water and the surface of kerogen increases, resulting in enhanced water wettability. To quantitatively characterize the changes in wettability, we used geometric methods to measure the CA on the surface of kerogen (Fig. 5).

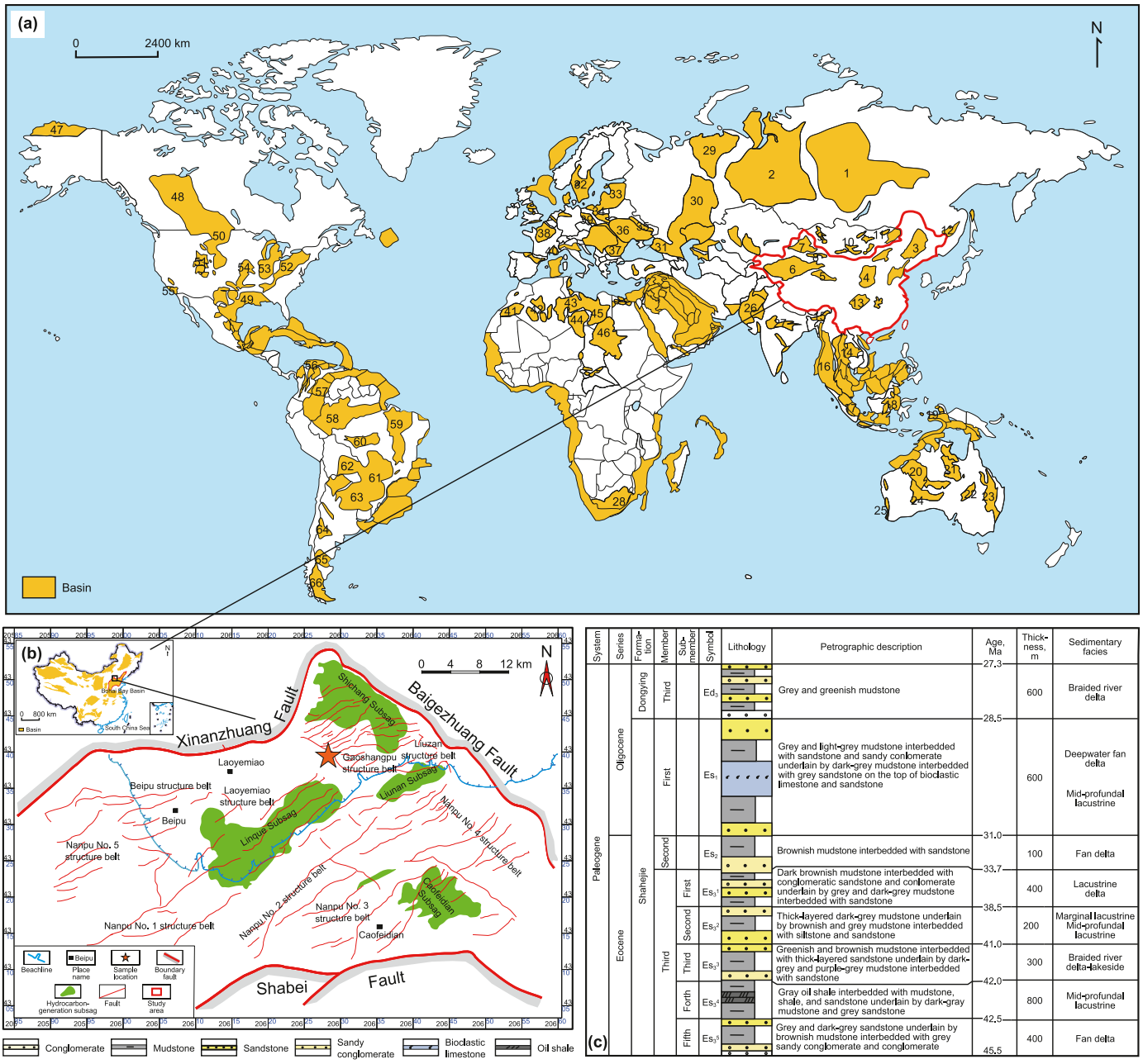

1-East Siberian Basin
2-West Siberian Basin
3-Songliao Basin
4-Erdos Basin
5-Qaidam Basin
6-Tarim Basin
7-Junggar Basin
8-Tuha Basin
9-Great Lake Basin
10-Central-South-East Basin
11-Hailar Basin
12-Middle Amur Basin
13-Southern China
14-Khorat Plateau Basin
15-Assam Basin
16-Chao Phraya River Basin
17-Central-South Sumatra Basin
18-Kute Basin
19-Bintuni Basin
20-Canning Basin
21-Georgina Basin
22-Erromanga Basin
23-Bonn-Sulate Basin
24-Orphesus-Amatius Basin
25-Perth Basin
26-Indus Basin
27-Wendia Basin
28-Karoo Basin
29-Timan-Pechora Basin
30-Volga-Ural Basin
31-North Caucasus Basin
32-Norway-Denmark Basin
33-Baltic Basin
34-Northeast Germany-Poland Basin
35-Dnieber-Donnets Basin
36-Pannon-North Carpathian Basin
37-South Carpathian Basin
38-Paris Basin
39-Turingen Basin
40-Provence Basin
41-Tindouf Basin
42-Tinimont/Ahnet Basin
43-Triassic-Gudamis-Iliz Basin
44-Muzuk Basin
45-Hilte Basin
46-Kufra Basin
47-Alaska North Slope Basin
48-Alberta Basin
49-Gulf of Mexico
50-Williston Basin
51-Rocky Mountains, USA
52-Appalachian Foreland-Black Warrior Basin
53-Michigan-Illinos Basin
54-Forest City-Chernokee Basin
55-San Joaquin Basin
56-Maracaibo Basin
57-Barinas-Apuer-Yanos Basin
58-Upper Amazon-Amazon Basin
59-Barnabas-Sint Francisco Basin
60-Paresis Basin
61-Barana Basin
62-Chakao-Cretaceous Basin
63-Chaco-baras Basin
64-Neuquen Basin
65-St. George Basin
66-Magallenas Basin

Fig. 2. (**a**) Global shale oil basin distribution (modified after Shi et al., 2024), (**b**) regional structural map of the Nanpu Sag area, and (**c**) comprehensive stratigraphic column of Nanpu Sag (modified after Chen et al., 2021).

We can observe that at CO_2 pressures of 10 and 20 MPa and temperatures of 298 and 313 K, the CA on the surface of kerogen is greater than 105°, indicating that the kerogen is wetted with CO_2. The CA between 105° and 180° was CO_2 wetting (Fanchi, 2005). At CO_2 pressures of 10 and 20 MPa and temperatures of 323 and 343 K, the CA on the surface of kerogen is between 75° and 105°, indicating kerogen neutral wetting; at CO_2 pressure of 5 MPa and temperatures of 298, 313, 323, and 343 K, the CA on the surface of kerogen is between 75° and 105°, indicating neutral kerogen wetting (Fanchi, 2005). The above conclusions are roughly the same as

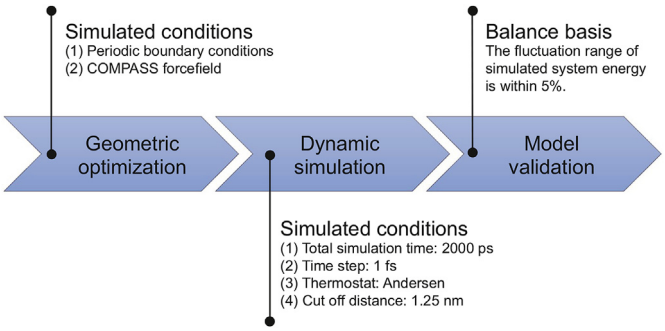

Fig. 3. Simulation calculation steps and simulation conditions.

those obtained by Yu et al. (2020) and Shi et al. (2022) through MD. We also compared the above conclusions with the experimental results of Pan et al. (2018), and the results were very similar, confirming the accuracy of the results obtained through simulation (Fig. 5).

We also plotted the relative concentration curves of water on the surface of kerogen at 5 MPa and different temperatures (Fig. 6). When the pressure is constant, the relative concentration increases with temperature, indicating an enhanced interaction between water and kerogen and enhanced water wettability.

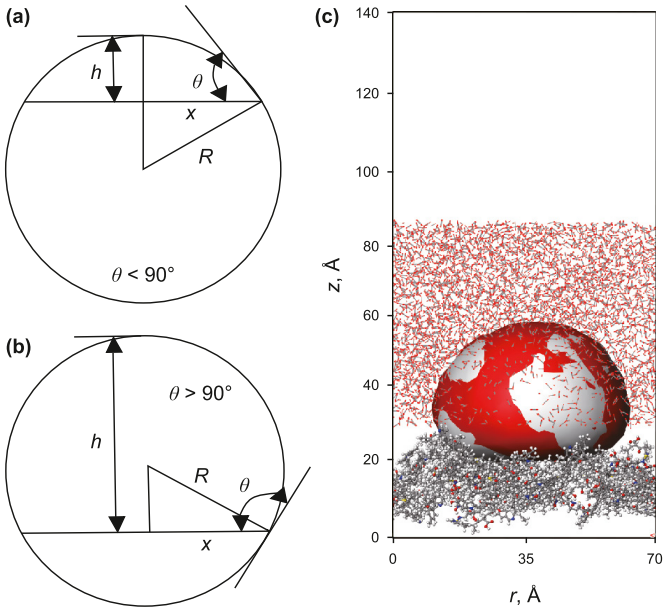

Fig. 4. Schematic diagram of a geometric method for calculating wetting angle: (**a**) sharp angle, (**b**) obtuse angle, and (**c**) isodensity model of water on the surface of cheese roots.

3.2. Influence of CO_2 pressure on wettability

We used MD to simulate the variation characteristics of the CA of the surface of kerogen at 5, 10, and 20 MPa. From Fig. 5, when the temperature remains constant, with a gradual increase of CO_2 pressure, the CA gradually increases and the water wettability gradually weakens. The influence of supercritical pressure on the wettability is crucial. At pressures below 7.375 MPa (critical pressure), water at 298, 313, 323, and 343 K is neutral wetting on the surface of kerogen (Fig. 7). When the pressure exceeds 7.375 MPa and the temperature is 298 and 313 K, the surface of kerogen changes from neutral wetting to CO_2 wetting, resulting in a wetting reversal. The critical pressure of CO_2 is 7.375 MPa (Bachu, 2000). In the supercritical state, CO_2 exhibits properties similar to both gas and liquid. Near the critical point, the physical properties of CO_2 undergo significant changes. These changes will affect the interactions between CO_2, kerogen, and surrounding fluids. Specifically, when the pressure exceeds the critical point, the density of CO_2 approaches that of the surrounding liquid phase, thereby reducing interfacial tension and altering the adhesion force at the

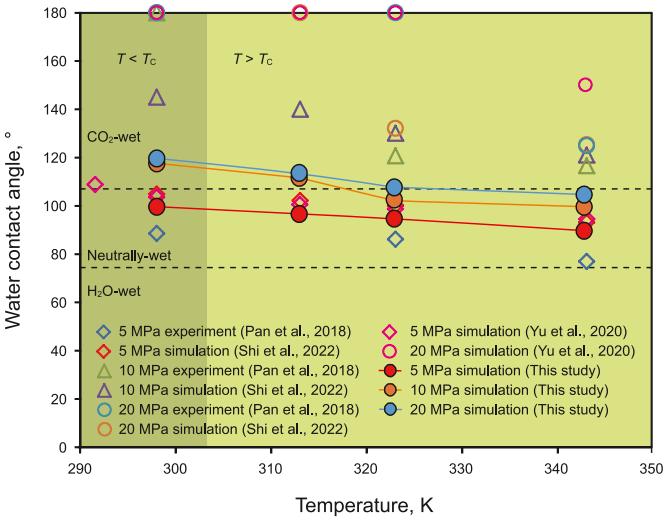

Fig. 5. CA on kerogen surface obtained from experiments and simulations at different temperatures.

Table 1
Simulation parameters.

Simulation modules	Parameter	Input	Unit
Amorphous cell-packing	Density of water box	1.000	g/cm^3
	Density of CO_2 box	1.101	g/cm^3
	Density of kerogen	1.106	g/cm^3
	Density of the entire system	0.521	g/cm^3
	Loading steps	1000	/
Geometry optimization	Maximum number of iterations	500	/
	Algorithm	Steepest descent	/
Dynamics	Time step	1	fs
	Ensemble	NVT	/
	Total simulation time	2000	ps
	Number of steps	2000000	/
	Thermostat	Andersen	/
	Frame output every	500	steps
	Initial velocities	Random	/

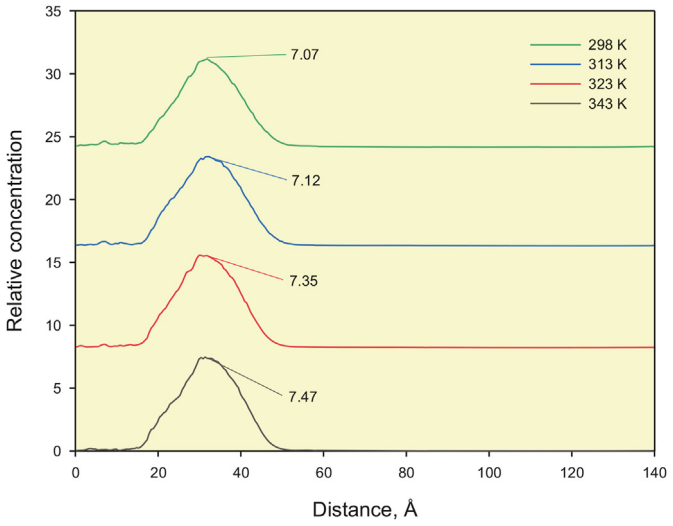

Fig. 6. Relative concentrations of water on kerogen surface under 5 MPa.

solid–liquid interface. This phenomenon explains the observed changes in wettability and highlights the importance of the critical pressure point in understanding CS behavior. The above conclusions are roughly the same as those obtained by Yu et al. (2020) and Shi et al. (2022) through MD. We also compared the above conclusions with the experimental results of Pan et al. (2018), and the results were very similar.

3.3. Influence of salinity on wettability

The salinity of underground fluids can affect the interaction between liquids and minerals, thereby affecting the wettability of minerals. We used a solution containing Na^+, Ca^{2+}, and Mg^{2+} to study the effect of salinity. As the $CaCl_2$ solution concentration increases, the CA increases (99°±2°, 104°±2°, and 114°±2°) (Fig. 8), and the hydrophilicity gradually weakens. As the salinity increases, kerogen wettability in NaCl and $MgCl_2$ solutions also changes similarly (Fig. 8). The above conclusions are roughly the same as those obtained by Yu et al. (2020) and Shi et al. (2022) through MD.

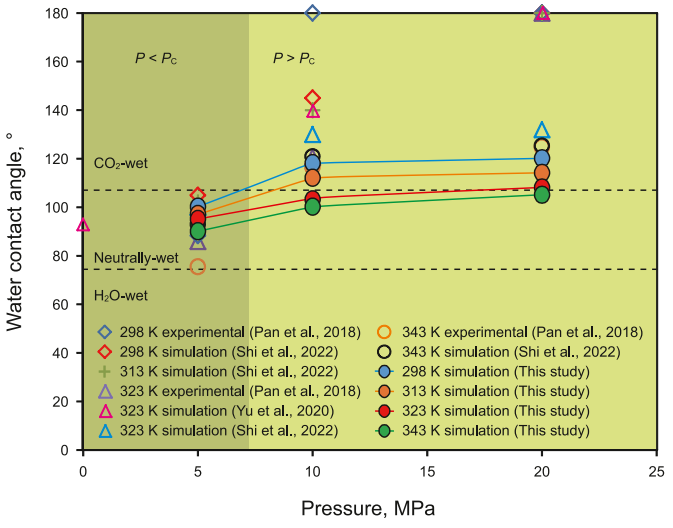

Fig. 7. CA on kerogen surface obtained from experiments and simulations under different pressures.

The ion type also significantly influences changes in the CA on the surface of kerogen (Fig. 8). $MgCl_2$ and NaCl solutions, respectively, have the greatest and smallest impact on kerogen wettability. The effect of $CaCl_2$ solution on kerogen wettability is moderate. Divalent cations (Mg^{2+} and Ca^{2+}) have a greater impact on wettability than monovalent cations (Na^+). This is consistent with the conclusions drawn by previous researchers using zeta potential experiments (Kasha et al., 2015; Alroudhan et al., 2016).

4. Discussion

4.1. Influence of CO_2–brine–kerogen wettability on CS

In this section, we discuss how to improve the efficiency of CS technology in field applications using the factors influencing wettability in CO_2–brine–shale systems. When the pressure increases to above 7.375 MPa or the temperature decreases, the shale becomes more CO_2 wetting, indicating a stronger interaction between CO_2 and shale (Chiquet et al., 2007). In addition, we simulated the wettability of kerogen without CO_2 and compared it with that of kerogen with CO_2. We found that the presence of CO_2 can weaken the hydrophilicity of the surface of kerogen (Fig. 9). Huang et al. (2018) reported that when the pressure increased to 7.375 MPa, the amount of CO_2 adsorbed on the surface of kerogen in shale reached its maximum. Later, experiments proved that the reason for this phenomenon was the affinity between CO_2 and kerogen. This affinity can effectively increase the adsorption capacity of CO_2. Therefore, in the early stages, higher pressure should be used. As the pressure rises to 7.375 MPa and the temperature decreases, the CS capacity reaches its maximum. Moreover, with an increase in salinity, wettability weakens. Therefore, when pressurizing, the salinity of underground fluids can also be appropriately increased to improve the CS capacity.

Storage safety is also controlled by the ability of the cap rock to retain CO_2 for a long time. The injected CO_2 will rise to the reservoir top through buoyancy and accumulate below the cap rock (Fig. 10). The pressure increase and temperature decrease caused by continuous CO_2 injection not only transform shale from water wetting to CO_2 wetting but also increase the permeability of the cap rock, which is not conducive to CS (Qin et al., 2022). When the CO_2 pressure rises above the breakthrough pressure, CO_2 leakage will occur. The breakthrough pressure is the maximum CS pressure in the reservoir. Therefore, when determining CO_2 pressure, not only the storage amount but also the storage safety should be

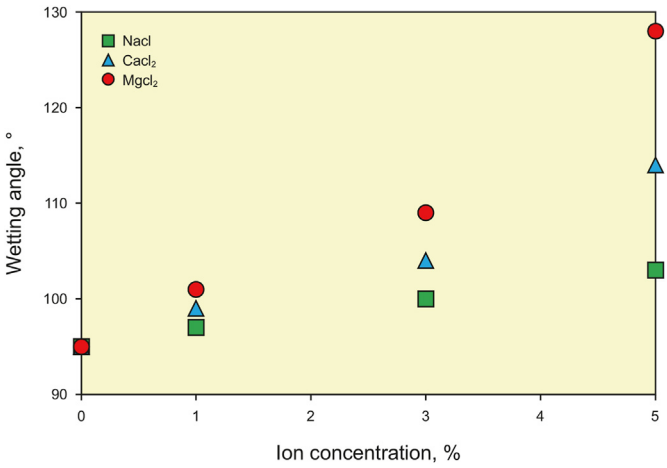

Fig. 8. CA changes with different salinities and ion types.

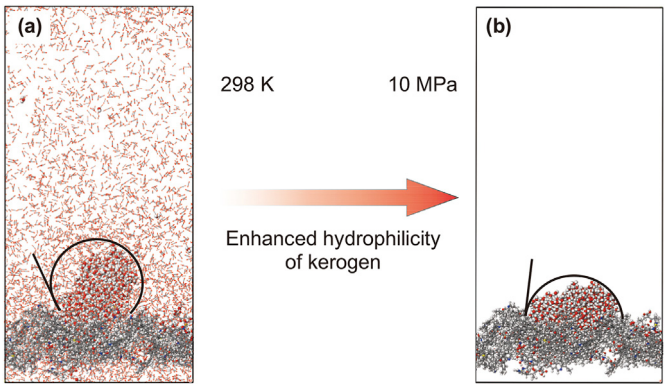

Fig. 9. Comparison of wettability between kerogen containing CO_2 and those without CO_2.

considered. There is a complex relationship between ion concentration, pressure, and storage risk in the study of CS safety. High ion concentration contributes to mineral sequestration, but may cause salt precipitation or pore blockage, increasing reservoir uncertainty (Pruess and Müller, 2009). High pressure can increase the density of CO_2, reduce the required storage space, but at the same time may pose a risk of reservoir rupture or crack propagation (Song and Zhang, 2012). Therefore, the selection of ion concentration and pressure needs to strike a balance between storage efficiency and safety. This study proposes a strategy for appropriately reducing pressure in high salinity reservoirs through a combination of experiments and simulations, in order to reduce the risk of salt precipitation while ensuring storage efficiency. This provides comprehensive analysis and optimization suggestions for the safe sequestration of CO_2.

In the practical application of CS technology, there are various potential challenges, including the long-term stability of wettability under extreme conditions, the need for experimental verification of simulation results, the economic feasibility of technology implementation, and the potential impact on the environment. For example, although this study investigated the effects of factors such as temperature, pressure, salinity, and ions on wettability, further research is needed to determine whether wettability can maintain consistency and stability under extreme conditions such as ultra-high pressure, strong acidity, or prolonged operation. Economic costs and environmental impacts are also key factors, and the widespread application of CS technology requires a balance between cost-effectiveness and environmental protection, balancing the short–term investment and long–term benefits of technology implementation (Ali et al., 2022b; Davoodi et al., 2024). To address these challenges, we suggest combining multi–scale simulations and experimental validation, utilizing theoretical models and experimental results from different scales to complement each other, in order to enhance the comprehensiveness and practical guidance of the research. At the same time, material optimization design, such as developing functional nanomaterials or surface modification technologies, can be used to improve the tolerance and performance of storage systems under extreme conditions. In addition, policy support and cost optimization analysis are also important directions. By formulating relevant incentive policies, promoting research and development investment, and implementing full lifecycle cost analysis, CS can ensure good economic feasibility and environmental sustainability (Alphen et al., 2010; Stechow et al., 2011; Wu and Wang, 2022). Through these measures, it is expected to overcome existing technological bottlenecks and further promote the practical application and promotion of CS technology.

4.2. System stability

4.2.1. Changes in kinetic energy

In MD simulations, kinetic energy can be used to describe system stability (Shi et al., 2023). The final equilibrium simulation can obtain the trajectory information of the velocity and position of each particle with time, which is the basis for subsequent data processing and analysis. It is necessary to analyze the system energy variation curves over time during the simulation process. If the energy fluctuation range is within 5%, the system is considered to have reached a stable state. By selecting the curves of kinetic energy with time in four temperature-simulated systems, it is clear that

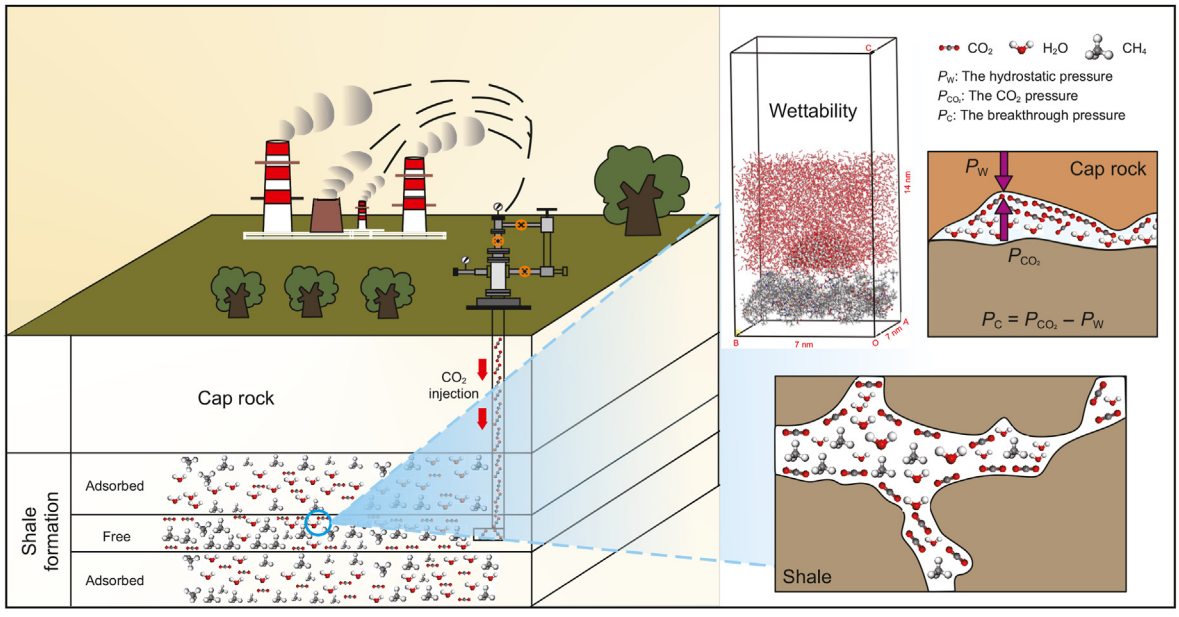

Fig. 10. Schematic diagram of the influence of CO_2–brine–kerogen wettability on CS in shale.

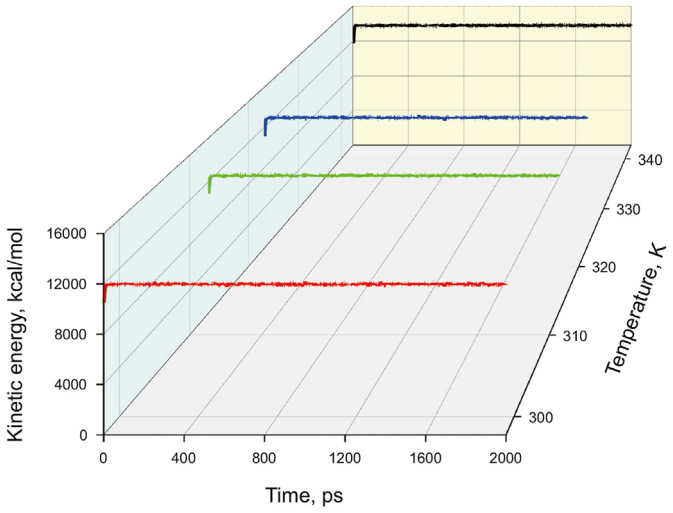

Fig. 11. Variation of kinetic energy in the CO_2–brine–kerogen wetting system with simulation time.

the simulated time is sufficient to achieve a stable state of the studied system (Fig. 11).

4.2.2. RDF analysis

The RDF typically represents the probability of finding other particles at a certain distance from a reference particle, given the position of that particle (Trokhymchuk et al., 2006). RDF is a function often used to judge whether a system is balanced. RDF is particularly suitable for liquids. With an increase in simulation time, the peak gradually decays and eventually equals 1 to judge whether the system reaches equilibrium; otherwise, the simulation time should be extended. Our system reached a stable state, and our simulation time was sufficiently long (Fig. 12).

RDF can also describe the affinity between atoms (Firooz et al., 2021). A higher peak value in the RDF indicates a stronger the interaction between H_2O and atoms on the surface of kerogen (Wang and Huang, 2019). Fig. 12 shows the RDF between water and single atoms in kerogen at the same temperature and pressure. The RDF between H_2O and N atoms in kerogen is higher than that between H_2O and other atoms, indicating that the substitution sites

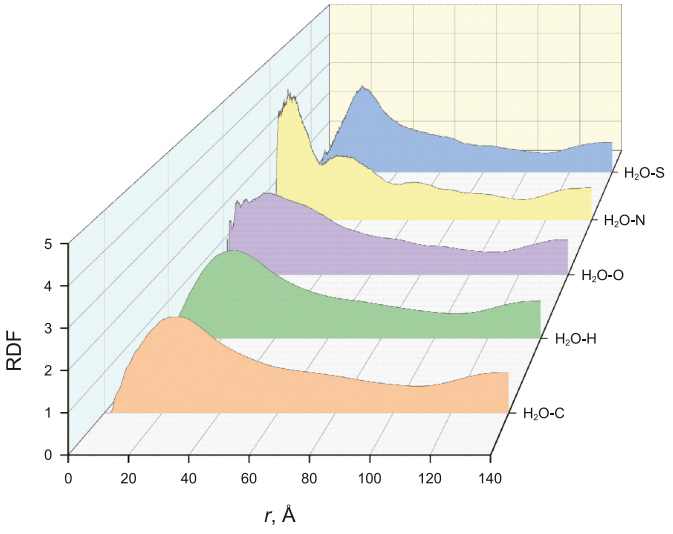

Fig. 12. RDF between H_2O and atoms in kerogen at 5 MPa and 298 K.

around N atoms in kerogen are high-energy sites for H_2O. This finding aligns with the conclusions of Lawal et al. (2020), who employed the B3LYP/Def2-TZVP theoretical level. It can be inferred that the interaction between H_2O and N in kerogen is stronger than those between H_2O and C, H, O, and S. Under these temperature and pressure conditions, water preferentially adsorbs at N atom positions in kerogen.

4.3. MSD and self-diffusion coefficient (D) analysis

Because MSD and D can be used to analyze the motion state of molecules, we used Materials Studio software to calculate the MSD and D of water in the system after running the kinetic model (Firooz et al., 2021; Tirjoo et al., 2019). As the simulation progressed, MSD gradually increased while D gradually decreased and then approached equilibrium (Fig. 13). This phenomenon can be attributed to the adsorption dynamics during the early stages of the simulation, where a significant amount of H_2O adsorbed onto the kerogen surface, leading to a high diffusion coefficient (D). As the simulation progressed, only the remaining H_2O suspended in CO_2 continued to diffuse, causing D to naturally decrease. In addition, the influence of temperature on D is very significant (Firooz et al., 2021). As the temperature increases, the diffusion of H_2O on the surface of kerogen gradually strengthens and the adsorption becomes faster, resulting in a larger D. The D value of H_2O is 343, 323, 313, and 298 K. This is consistent with the previously obtained results through MD (Zhao and Jin, 2020).

$$\mathrm{MSD} = \frac{1}{N}\sum_{i=1}^{N}[r_i(t) - r_i(0)]^2 \tag{6}$$

$$D = \frac{1}{6N}\lim_{t\to\infty}\frac{\mathrm{d}}{\mathrm{d}t}\sum_{i=1}^{N}[r_i(t) - r_i(0)]^2 = \frac{1}{6}K_{\mathrm{MSD}} \tag{7}$$

where N denotes the number of diffusion molecules, $r(t)$ and $r(0)$ denote the position vectors of molecules at t and $t = 0$ respectively, and K_{MSD} denotes the slope of the MSD curve.

4.4. Interaction energy

In the simulation process, the interaction energy can reflect the interactions between molecules. After the MD simulation, we analyzed the difference between the interaction energies between CO_2 and kerogen ($E_{\mathrm{C\text{-}K}}$) and between H_2O and kerogen ($E_{\mathrm{W\text{-}K}}$) (Fig. 14) (Ma et al., 2019).

$$E_{\mathrm{C-K}} = E_{\mathrm{C+K}} - E_{\mathrm{C}} - E_{\mathrm{K}} \tag{8}$$

where $E_{\mathrm{C+K}}$ denotes the energy of CO_2 and kerogen surface, kcal/mol; E_{C} denotes the energy of CO_2, kcal/mol; E_{K} denotes the energy of kerogen surface, kcal/mol.

$$E_{\mathrm{W-K}} = E_{\mathrm{W+K}} - E_{\mathrm{W}} - E_{\mathrm{K}} \tag{9}$$

where $E_{\mathrm{W+K}}$ denotes the energy of H_2O and kerogen surface, kcal/mol; E_{W} denotes the energy of H_2O, kcal/mol.

$$\Delta E = E_{\mathrm{C-K}} - E_{\mathrm{W-K}} \tag{10}$$

Previous studies have shown that when ΔE is negative, CO_2 adsorption on the kerogen is stronger than H_2O adsorption and kerogen is more CO_2-friendly (Zhong et al., 2013). ΔE values are negative at different temperatures, indicating that kerogen is CO_2 wetted (Fig. 14). In addition, as the temperature increases, ΔE

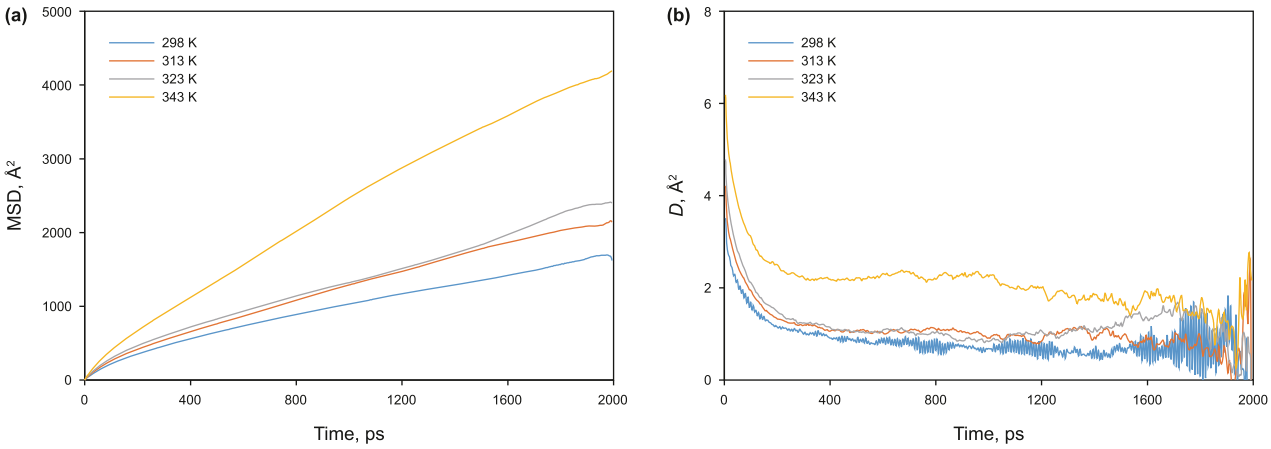

Fig. 13. MSD and D of H_2O on kerogen surface under 5 MPa.

gradually decreases, and CO_2 wettability on the surface of kerogen gradually weakens. The results above align with those obtained by Tao et al. (2024) using MD simulations and with the conclusions drawn in Section 3.1. Under actual reservoir conditions, the interaction between CO_2 and H_2O molecules significantly affects the wettability transition and reservoir pore structure. CO_2 tend to adsorb on the surface of kerogen, while H_2O is more likely to aggregate in hydrophilic regions. This distribution change will alter the wettability of the reservoir surface, thereby affecting the permeability and distribution stability of CO_2. And under high pressure and high water content conditions, CO_2 adsorption may lead to chemical dissolution or precipitation on the surface of reservoir pores, which can change the porosity and permeability of the reservoir, thereby affecting long−term stability.

4.5. Electrostatic potential energy

Throughout the MD simulation, electrostatic potential energy serves as an indicator of the interactions between molecules and the overall charge distribution within the system (Tao et al., 2024). The position and strength of hydrogen bond formation can be predicted by the electrostatic potential energy of molecules. Therefore, electrostatic potential energy analysis is crucial for studying the interaction between kerogen and H_2O (An et al., 2019). The molecular electrostatic potential energy was calculated using the DMol3 module (Tabari and Farmanzadeh, 2020). By analyzing the electrostatic potential energy of kerogen, its wetting mechanism was clarified. Fig. 15 shows the electrostatic potential energy distribution of H_2O, CO_2, and kerogen. The blue area in the

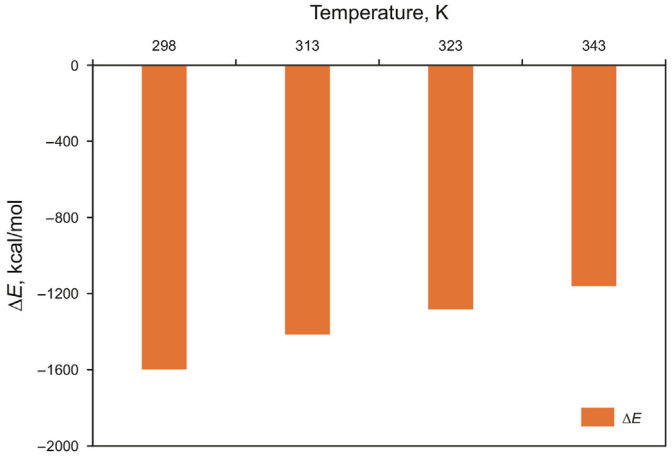

Fig. 14. ΔE at different temperatures.

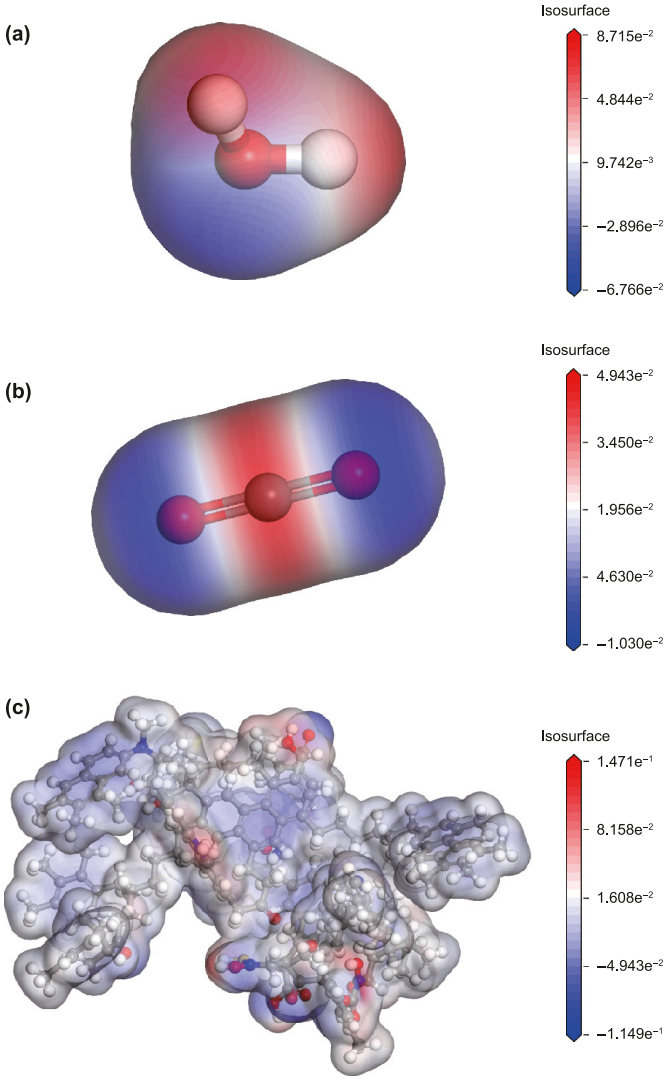

Fig. 15. Electrostatic potential energy spectra. (**a**) H_2O, (**b**) CO_2, and (**c**) kerogen.

Table 2
Maximum electrostatic potential energy of H_2O, CO_2, and kerogen.

Molecule type	Maximum positive potential	Maximum negative potential
H_2O	0.08715 au	−0.06766 au
CO_2	0.04943 au	−0.01030 au
Kerogen	0.1471 au	−0.1149 au

electrostatic potential energy diagram indicates negative charge, and the electron pairs in this area easily form hydrogen bonds. The red region is opposite to the blue region, and hydrogen bonds can be formed by accepting electrons (Gan et al., 2023). The maximum surface electrostatic potentials of various molecules are listed in Table 2. The maximum negative potential (−0.06766 au) of H_2O is located around the oxygen atom, and the maximum positive potential (0.08715 au) is distributed around the hydrogen atom (Fig. 15(a)). The maximum negative potential (−0.01030 au) of CO_2 is located around the oxygen atom, and the maximum positive potential (0.04943 au) is distributed around the carbon atom (Fig. 15(b)). In the kerogen model, the blue region is mainly distributed near the oxygen atom (Fig. 15(c)). A larger difference in electrostatic potential energy between molecules indicates stronger molecular interactions (Zhao et al., 2023). CO_2 is more likely to form hydrogen bonds on the surface of kerogen and absorb them than H_2O, which is consistent with the results obtained in Section 4.4.

4.6. Hydrogen bond analysis

The strongest interaction between H_2O and kerogen is promoted by hydrogen bonds, in which H_2O is the donor and heteroatoms (N, O, and S) in kerogen are the acceptors (Zhou et al., 2022). To further reveal the change of water wettability of the surface of kerogen with temperature, we analyzed the number of hydrogen bonds formed between H_2O and the surface of kerogen at different temperatures and pressures. Using the geometric criterion proposed by Kumar et al. (2007), if the distance between the donor and receptor is less than 0.3 nm, and the angle between them is between 90° and 180° (O–H–O), there is a hydrogen bond.

The total number of hydrogen bonds gradually increases with increasing temperature (Fig. 16(a)) and decreases with increasing pressure (Fig. 16(b)). At 298 K, 5 MPa, the number of hydrogen bonds between donor and receptor lengths of 1.68–1.76 Å is the largest (Fig. 16(c)). When the hydrogen bond length is less than 2.3 Å, the first layer of water forms a hydrogen bond interaction with kerogen. When the hydrogen bond length is greater than 2.3 Å, the second layer of water forms a hydrogen bond interaction with kerogen. The shorter the hydrogen bond length, the stronger the interaction between H_2O and the surface of kerogen. At 298 K, 5 MPa, the number of hydrogen bonds between the donor and receptor at an angle of 150°–170° is the largest (Fig. 16(d)). The results showed that the hydrophily of the surface of kerogen increased with temperature (Fig. 16). In addition, with an increase in pressure, the hydrophily of the surface of kerogen gradually weakens, which is conducive to CO_2 storage.

4.7. Force analysis

The van der Waals force is an electronic attraction that occurs between molecules with different electronic configurations and becomes significant when atoms or molecules are in close proximity (Seyyedattar et al., 2019; Ebrahimi, 2014; Lennard-Jones, 1924; Klein, 1974). The fluctuation of the atomic electron cloud makes an atom have an instantaneous electric dipole moment. This dipole moment can induce neighboring atoms to develop their own dipole moments, leading to attractive interactions between these

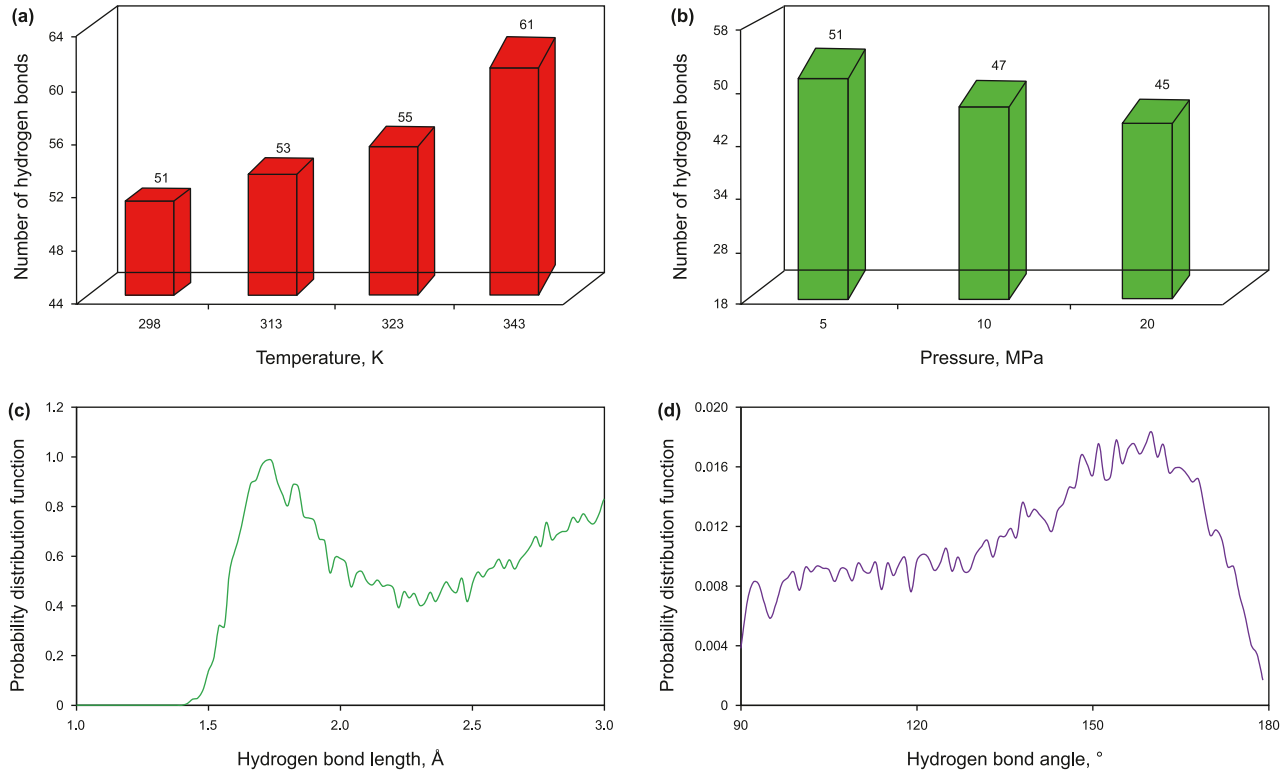

Fig. 16. Number of hydrogen bonds between H_2O and kerogen at different temperatures (**a**) and CO_2 pressures (**b**). Probability distribution function of hydrogen bond length (**c**) and angle (**d**) at 298 K, 5 MPa.

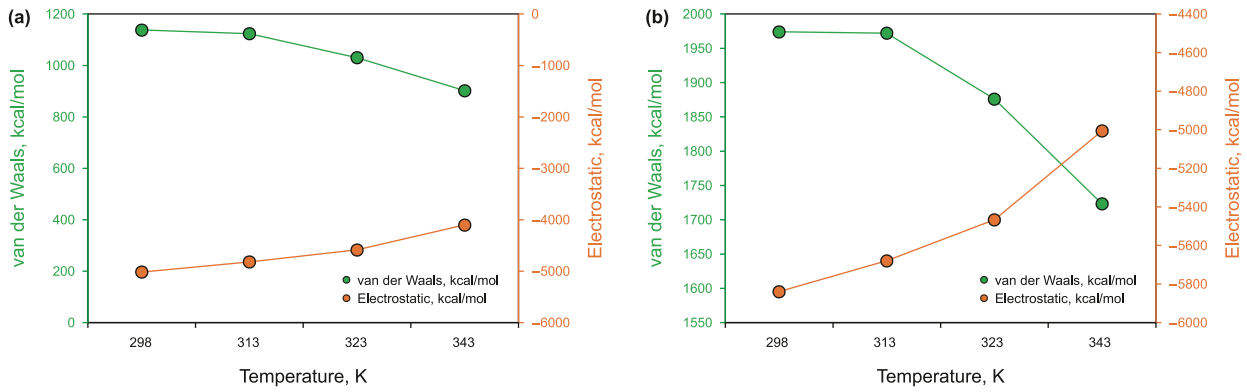

Fig. 17. van der Waals force and electrostatic force at different temperatures: (**a**) H_2O and (**b**) H_2O and kerogen.

induced dipoles (Visser, 1989). While van der Waals forces are commonly associated with interactions between nonpolar molecules, they can also occur between polar molecules. These forces arise from temporary dipole moments in nonpolar molecules and contribute to the overall intermolecular interactions. The van der Waals force between H_2O and kerogen is greater than that between water molecules; thus, H_2O will gradually approach the surface of kerogen with increasing simulation time (Fig. 17).

Electrostatic force acts between two charged particles, with like charges repelling each other and opposite charges attracting each other (Cao et al., 2021). In the MD simulation process, the charge between kerogen and H_2O remains constant, so distance is an important factor influencing the electrostatic force. As the temperature increases, the hydrophilicity of kerogen increases, the distance between kerogen and H_2O decreases, and the electrostatic force gradually increases (Fig. 17).

5. Conclusions

(1) Supercritical conditions are crucial for determining of wettability. The kerogen surface becomes more hydrophilic as temperature rises. At CO_2 pressures of 10 and 20 MPa, with an increase in temperature, kerogen changes from CO_2 wetting to neutral wetting. When the CO_2 pressure is 5 MPa, kerogen is neutral wetting. When the temperature remains constant, with a gradual increase in pressure, the hydrophily on the surface of kerogen gradually weakens. At pressures below 7.375 MPa, the wettability on the surface of kerogen is neutral wetting. When the pressure exceeds 7.375 MPa and the temperature is 298 and 313 K, the water wettability on the surface of kerogen changes from neutral wetting to CO_2 wetting, resulting in a wetting reversal. Ion concentration has a certain effect on kerogen wettability. Divalent cations have a greater impact on wettability than monovalent cations. With an increase in salinity, hydrophily decreases.

(2) Through RDF, we determined that water is preferentially adsorbed at N atom positions in kerogen. The interaction energy between CO_2 and the kerogen is greater than that between H_2O and the surface of kerogen. The greater the electrostatic potential energy difference between molecules, the greater the interaction between molecules, and CO_2 forms more hydrogen bonds on the surface of kerogen and is adsorbed than H_2O. The surface of kerogen is CO_2 wetting. The number of hydrogen bonds between H_2O and kerogen gradually increases with increasing temperature and decreases with increasing pressure. The van der Waals force between H_2O and kerogen is greater than that between H_2O molecules; thus, the hydrophilicity of the surface of kerogen increases with simulation time.

(3) At an early stage, a higher CO_2 pressure should be used. When the pressure rises to 7.375 MPa and the temperature is low, the CO_2 storage capacity reaches its maximum. When pressurizing, the salinity of underground fluids can also be appropriately increased to improve CS. Notably, when determining CO_2 pressure, not only the storage amount but also storage safety should be considered.

CRediT authorship contribution statement

Kan-Yuan Shi: Writing – original draft, Investigation, Funding acquisition, Conceptualization. **Jun-Qing Chen:** Writing – review & editing, Supervision, Software, Methodology, Funding acquisition. **Xiong-Qi Pang:** Writing – review & editing, Resources, Project administration, Methodology, Funding acquisition. **Sha-Sha Hui:** Resources, Formal analysis, Data curation, Conceptualization. **Zhang-Xin Chen:** Writing – review & editing, Supervision, Software, Methodology. **Ben-Jie-Ming Liu:** Methodology, Investigation, Formal analysis, Data curation. **Yu-Jie Jin:** Resources, Methodology, Investigation. **Si-Jia Zhang:** Resources, Methodology, Investigation.

Declaration of competing interest

The authors declare that they have no known competing financial interests or personal relationships that could have appeared to influence the work reported in this paper.

Acknowledgements

This work was supported by the China Scholarship Council (Grant No. 202306440152); the CNPC Science and Technology Major Project of the Fourteenth Five-Year Plan (Grant No. 2021DJ0101); the Science Foundation of China University of Petroleum, Beijing (Grant No. 2462022YXZZ007), and the National Natural Science Foundation of China (Grant No. 42102145).

References

Alder, B.J., Wainwright, T.E., 1957. Phase transition for a hard sphere system. J. Chem. Phys. 27 (5), 1208–1209. https://doi.org/10.1063/1.1743957.

Ali, F., Negash, B.M., Ridha, S., et al., 2023. A review on the interfacial properties of caprock/CO_2/brine system-implications for structural integrity of deep saline aquifers during geological carbon storage. Earth Sci. Rev. 247, 104600. https://doi.org/10.1016/j.earscirev.2023.104600.

Ali, F., Negash, B.M., Ridha, S., et al., 2024. Wettability alterations of amorphous shales in geological carbon storage: impact of acidic conditions in deep saline

aquifers. Geoenergy Science and Engineering 234, 212612. https://doi.org/10.1016/j.geoen.2023.212612.
Ali, M., Pan, B., Yekeen, N., et al., 2022a. Assessment of wettability and rock-fluid interfacial tension of caprock: implications for hydrogen and carbon dioxide geo-storage. Int. J. Hydrogen Energy 47 (30), 14104–14120. https://doi.org/10.1016/j.ijhydene.2022.02.149.
Ali, M., Jha, N.K., Pal, N., et al., 2022b. Recent advances in carbon dioxide geological storage, experimental procedures, influencing parameters, and future outlook. Earth Sci. Rev. 225, 103895. https://doi.org/10.1016/j.earscirev.2021.103895.
Alphen, K.V., Noothout, P.M., Hekkert, M.P., et al., 2010. Evaluating the development of carbon capture and storage technologies in the United States. Renew. Sustain. Energy Rev. 14 (3), 971–986. https://doi.org/10.1016/j.rser.2009.10.028.
Al-Raeei, M., El-Daher, M.S., 2019. A numerical method for fractional Schrodinger equation of Lennard-Jones potential. Phys. Lett. 383 (26), 125831. https://doi.org/10.1016/j.physleta.2019.07.019.
Alroudhan, A., Vinogradov, J., Jackson, M.D., 2016. Zeta potential of intact natural limestone: impact of potential-determining ions Ca^{2+}, Mg^{2+} and SO_4^{2-}. Colloid Surf. A-Physicochem. Eng. Asp. 493, 83–98. https://doi.org/10.1016/j.colsurfa.2015.11.068.
Al-Yaseri, A., Abdel-Azeim, S., Al-Hamad, J., 2023. Wettability of water-H_2-quartz and water-H_2-calcite experiment and molecular dynamics simulations: critical assessment. Int. J. Hydrogen Energy 48 (89), 34897–34905. https://doi.org/10.1016/j.ijhydene.2023.05.294.
Al-Yaseri, A., Abdulelah, H., Yekeen, N., et al., 2021. Assessment of CO_2/shale interfacial tension. Colloid Surf. A-Physicochem. Eng. Asp. 627, 127118. https://doi.org/10.1016/j.colsurfa.2021.127118.
An, X.J., Kang, Y., Li, G.S., 2019. The interaction between chitosan and tannic acid calculated based on the density functional theory. Chem. Phys. 520, 100–107. https://doi.org/10.1016/j.chemphys.2018.12.009.
Andersen, H.C., 1980. Molecular dynamics simulations at constant pressure and/or temperature. J. Chem. Phys. 72 (4), 2384–2393. https://doi.org/10.1063/1.439486.
Awolayo, A., Sarma, H., AlSumaiti, A., 2016. An experimental investigation into the impact of sulfate ions in smart water to improve oil recovery in carbonate reservoirs. Transport Porous Media 111 (3), 649–668. https://doi.org/10.1007/s11242-015-0616-4.
Bachu, S., 2000. Sequestration of CO_2 in geological media: criteria and approach for site selection in response to climate change. Energy Convers. Manag. 41 (9), 953–970. https://doi.org/10.1016/S0196-8904(99)00149-1.
Bhattacharjee, S., Khan, S., 2019. Effect of alkyl chain length on the wetting behavior of imidazolium based ionic liquids: a molecular dynamics study. Fluid Phase Equilib. 501, 112253. https://doi.org/10.1016/j.fluid.2019.112253.
Birkholzer, J.T., Oldenburg, C.M., Zhou, Q.L., 2015. CO_2 migration and pressure evolution in deep saline aquifers. Int. J. Greenh. Gas Control 40, 203–220. https://doi.org/10.1016/j.ijggc.2015.03.022.
Cao, Z., Jiang, H., Zeng, J.H., et al., 2021. Nanoscale liquid hydrocarbon adsorption on clay minerals: a molecular dynamics simulation of shale oils. Chem. Eng. J. 420, 127578. https://doi.org/10.1016/j.cej.2020.127578.
Chakraborty, T., Hens, A., Kulashrestha, S., et al., 2015. Calculation of diffusion coefficient of long chain molecules using molecular dynamics. Physica 69, 371–377. https://doi.org/10.1016/j.physe.2015.01.008.
Chang, X., Xue, Q.Z., Li, X.F., et al., 2018. Inherent wettability of different rock surfaces at nanoscale: a theoretical study. Appl. Surf. Sci. 434, 73–81. https://doi.org/10.1016/j.apsusc.2017.10.173.
Chen, D., Pang, X.Q., Li, L., et al., 2021. Organic geochemical characteristics and shale oil potential of the middle Eocene early-mature shale in the Nanpu Sag, Bohai Bay Basin, Eastern China. Mar. Petrol. Geol. 133, 105248. https://doi.org/10.1016/j.marpetgeo.2021.105248.
Chiquet, P., Broseta, D., Thibeau, S., 2007. Wettability alteration of caprock minerals by carbon dioxide. Geofluids 7 (2), 112–122. https://doi.org/10.1111/j.1468-8123.2007.00168.x.
Davoodi, S., Al-Shargabi, M., Wood, D.A., et al., 2024. Carbon dioxide sequestration through enhanced oil recovery: a review of storage mechanisms and technological applications. Fuel 366, 131313. https://doi.org/10.1016/j.fuel.2024.131313.
Deng, P., Chen, Z.X., Peng, X.L., et al., 2023. Optimized lower pressure limit for condensate underground gas storage using a dynamic pseudo-component model. Energy 285, 129505. https://doi.org/10.1016/j.energy.2023.129505.
Ebrahimi, D., 2014. Multiscale Modeling of Clay-Water Systems. Massachusetts Institute of Technology.
Famoori, F., Azin, R., Osfouri, S., et al., 2021. Experimental investigation of the geochemical and mineralogical interaction between CO_2 and carbonate: evaluation of CO_2 sequestration in dolomite-calcite formations. Energy Clim. Change. 2, 100029. https://doi.org/10.1016/j.egycc.2021.100029.
Fanchi, J.R., 2005. Principles of Applied Reservoir Simulation. Elsevier.
Firooz, A.F., Hashemi, A., Zargar, G., et al., 2021. Molecular dynamics modeling and simulation of silicon dioxide-low salinity water nanofluid for enhanced oil recovery. J. Mol. Liq. 339, 116834. https://doi.org/10.1016/j.molliq.2021.116834.
Gan, J., Wang, D.M., Xiao, Z.M., et al., 2023. Experimental and molecular dynamics investigations of the effects of ionic surfactants on the wettability of low-rank coal. Energy 271, 127012. https://doi.org/10.1016/j.energy.2023.127012.
Gholami, R., Raza, A., Andersen, P., et al., 2021. Long-term integrity of shaly seals in CO_2 geo-sequestration sites: an experimental study. Int. J. Greenh. Gas Control 109, 103370. https://doi.org/10.1016/j.ijggc.2021.103370.
Heydari, M., Sharif, F., Ebrahimi, M., 2021. A molecular dynamics study on the role of oxygen-containing functional groups on the adhesion of polymeric films to the aluminum surface. Fluid Phase Equilib. 536, 112966. https://doi.org/10.1016/j.fluid.2021.112966.
Hu, T., Jiang, F.J., Pang, X.Q., et al., 2024. Identification and evaluation of shale oil micro-migration and its petroleum geological significance. Petrol. Explor. Dev. 51 (1), 127–140. https://doi.org/10.1016/s1876-3804(24)60010-8.
Hu, T., Liu, Y., Jiang, F.J., et al., 2023. A novel method for quantifying hydrocarbon micromigration in heterogeneous shale and the controlling mechanism. Energy 288, 129712. https://doi.org/10.1016/j.energy.2023.129712.
Hu, T., Pang, X.Q., Jiang, F.J., et al., 2022. Dynamic continuous hydrocarbon accumulation (DCHA): existing theories and a new unified accumulation model. Earth Sci. Rev. 232, 104109. https://doi.org/10.1016/j.earscirev.2022.104109.
Hu, Y.A., Devegowda, D., Sigal, R., 2016. A microscopic characterization of wettability in shale kerogen with varying maturity levels. J. Nat. Gas Sci. Eng. 33, 1078–1086. https://doi.org/10.1016/j.jngse.2016.06.014.
Huang, C., Tian, L., Wang, J.X., et al., 2024. Water-CO_2 wettability on sandstone surface with asphaltene adsorption: molecular dynamics simulation. Fuel 360, 130558. https://doi.org/10.1016/j.fuel.2023.130558.
Huang, L., Ning, Z.F., Wang, Q., et al., 2018. Effect of organic type and moisture on CO_2/CH_4 competitive adsorption in kerogen with implications for CO_2 sequestration and enhanced CH_4 recovery. Appl. Energy 210, 28–43. https://doi.org/10.1016/j.apenergy.2017.10.122.
Kasha, A., Al-Hashim, H., Abdallah, W., et al., 2015. Effect of Ca^{2+}, Mg^{2+} and SO_4^{2-} ions on the zeta potential of calcite and dolomite particles aged with stearic acid. Colloid Surf. A-Physicochem. Eng. Asp. 482, 290–299. https://doi.org/10.1016/j.colsurfa.2015.05.043.
Kassa, A.M., Gasda, S.E., Landa-Marbán, D., et al., 2022. Field-scale impacts of long-term wettability alteration in geological CO_2 storage. Int. J. Greenh. Gas Control 114, 103556. https://doi.org/10.1016/j.ijggc.2021.103556.
Kim, H., Makhnenko, R.Y., 2023. Characterization of multiphase flow in shaly caprock for geologic CO_2 storage. Adv. Water Resour. 182, 104570. https://doi.org/10.1016/j.advwatres.2023.104570.
Klein, M.J., 1974. The historical origins of the van der Waals equation. Physica 73 (1), 28–47. https://doi.org/10.1016/0031-8914(74)90224-9.
Kumar, R., Schmidt, J.R., Skinner, J.L., 2007. Hydrogen bonding definitions and dynamics in liquid water. J. Chem. Phys. 126 (20), 204107. https://doi.org/10.1063/1.2742385.
Lawal, L.O., Olayiwola, T., Abdel-Azeim, S., et al., 2020. Molecular simulation of kerogen-water interaction: theoretical insights into maturity. J. Mol. Liq. 299, 112224. https://doi.org/10.1016/j.molliq.2019.112224.
Lennard-Jones, J.E., 1924. On the determination of molecular fields. II. From the equation of state of gas. Proc. Roy. Soc. A. 106 (738), 463–477.
Li, J.C., Wang, F., 2017. Water graphene contact surface investigated by pairwise potentials from force-matching PAW-PBE with dispersion correction. J. Chem. Phys. 146 (5), 054702. https://doi.org/10.1063/1.4974921.
Lu, Y.Y., Tian, R.R., Tang, J.R., et al., 2021. Investigating the mineralogical and chemical effects of CO_2 injection on shale wettability at different reservoir temperatures and pressures. Energy Fuels 35 (18), 14838–14851. https://doi.org/10.1021/acs.energyfuels.1c01943.
Ma, Y., Lu, G.W., Shao, C.J., et al., 2019. Molecular dynamics simulation of hydrocarbon molecule adsorption on kaolinite (001) surface. Fuel 237, 989–1002. https://doi.org/10.1016/j.fuel.2018.10.063.
Pan, B., Jones, F., Huang, Z.Q., et al., 2019. Methane (CH_4) wettability of clay-coated quartz at reservoir conditions. Energy Fuels 33 (2), 788–795. https://doi.org/10.1021/acs.energyfuels.8b03536.
Pan, B., Li, Y.J., Wang, H.Q., et al., 2018. CO_2 and CH_4 wettabilities of organic-rich shale. Energy Fuels 32 (2), 1914–1922. https://doi.org/10.1021/acs.energyfuels.7b01147.
Pan, B., Yin, X., Iglauer, S., 2020. A review on clay wettability: from experimental investigations to molecular dynamics simulations. Adv. Colloid Interface Sci. 285, 102266. https://doi.org/10.1016/j.cis.2020.102266.
Pham, L.N., Walsh, T.R., 2021. Force fields for water-surface interaction: is reproduction of the experimental water contact angle enough? Chem. Commun. 57 (27), 3355–3358. https://doi.org/10.1039/d1cc00426c.
Pruess, K., Müller, N., 2009. Formation dry-out from CO_2 injection into saline aquifers: 1. Effects of solids precipitation and their mitigation. Water Resour. Res. 45 (3), W03402. https://doi.org/10.1029/2008WR007101.
Qin, C., Jiang, Y.D., Zhou, J.P., et al., 2022. Influence of supercritical CO_2 exposure on water wettability of shale: implications for CO_2 sequestration and shale gas recovery. Energy 242, 122551. https://doi.org/10.1016/j.energy.2021.122551.
Rego, F.B., Eltahan, E., Sepehrnoori, K., 2022. Wettability alteration and improved oil recovery in unconventional resources. J. Pet. Sci. Eng. 212, 110292. https://doi.org/10.1016/j.petrol.2022.110292.
Savin, A.V., Mazo, M.A., 2020. The COMPASS force field: validation for carbon nanoribbons. Physica 118, 113937. https://doi.org/10.1016/j.physe.2019.113937.
Seyyedattar, M., Zendehboudi, S., Butt, S., 2019. Molecular dynamics simulations in reservoir analysis of offshore petroleum reserves: a systematic review of theory

and applications. Earth Sci. Rev. 192, 194–213. https://doi.org/10.1016/j.earscirev.2019.02.019.
Shi, K.Y., Chen, J.Q., Pang, X.Q., et al., 2022. Effect of wettability of shale on CO_2 sequestration with enhanced gas recovery in shale reservoir: implications from molecular dynamics simulation. J. Nat. Gas Sci. Eng. 107, 104798. https://doi.org/10.1016/j.jngse.2022.104798.
Shi, K.Y., Chen, J.Q., Pang, X.Q., et al., 2023. Wettability of different clay mineral surfaces in shale: implications from molecular dynamics simulations. Pet. Sci. 20 (2), 689–704. https://doi.org/10.1016/j.petsci.2023.02.001.
Shi, K.Y., Chen, J.Q., Pang, X.Q., et al., 2024. Average molecular structure model of shale kerogen: experimental characterization, structural reconstruction, and pyrolysis analysis. Fuel 355, 129474. https://doi.org/10.1016/j.fuel.2023.129474.
Song, J., Zhang, D.X., 2012. Comprehensive review of caprock-sealing mechanisms for geologic carbon sequestration. Environ. Sci. Technol. 47 (1), 9–22. https://doi.org/10.1021/es301610p.
Stechow, C.V., Watson, J., Praetorius, B., 2011. Policy incentives for carbon capture and storage technologies in Europe: a qualitative multi-criteria analysis. Glob. Environ. Change-Human Policy Dimens. 21 (2), 346–357. https://doi.org/10.1016/j.gloenvcha.2011.01.011.
Sun, H., 1998. COMPASS: an ab initio force-field optimized for condensed-phase applications overview with details on alkane and benzene compounds. J. Chem. Phys. B. 102 (38), 7338–7364. https://doi.org/10.1021/jp980939v.
Sun, Y., Zuo, L., Li, X.L., et al., 2023. Enhancing shale gas recovery by carbon dioxide injection: a method of carbon capture, utilization and storage (CCUS). Process Saf. Environ. Prot. 179, 484–492. https://doi.org/10.1016/j.psep.2023.09.049.
Tabari, L., Farmanzadeh, D., 2020. Yttrium doped graphene oxide as a new adsorbent for H_2O, CO, and ethylene molecules: dispersion-corrected DFT calculations. Appl. Surf. Sci. 500, 144029. https://doi.org/10.1016/j.apsusc.2019.144029.
Tao, W.H., Jiang, B.Y., Zheng, Y.N., et al., 2024. Molecular dynamics study on the effect of inorganic salts on the wettability of surfactants on bituminous coal: sodium dodecyl sulfate and sodium chloride as representatives. Fuel 359, 130397. https://doi.org/10.1016/j.fuel.2023.130397.
Tirjoo, A., Bayati, B., Rezaei, H., et al., 2019. Molecular dynamics simulations of asphaltene aggregation under different conditions. J. Pet. Sci. Eng. 177, 392–402. https://doi.org/10.1016/j.petrol.2019.02.041.
Trokhymchuk, A., Nezbeda, I., Jirsák, J., et al., 2006. Hard sphere radial distribution function again. J. Chem. Phys. 124 (14), 149902. https://doi.org/10.1063/1.2188941.
Visser, J., 1989. Van der Waals and other cohesive forces affecting powder fluidization. Powder Technol. 58 (1), 1–10. https://doi.org/10.1016/0032-5910(89)80001-4.
Wang, E.Z., Feng, Y., Guo, T.L., et al., 2022a. Oil content and resource quality evaluation methods for lacustrine shale: a review and a novel three-dimensional quality evaluation model. Earth Sci. Rev. 232, 104134. https://doi.org/10.1016/j.earscirev.2022.104134.
Wang, E.Z., Li, C.R., Feng, Y., et al., 2022b. Novel method for determining the oil moveable threshold and an innovative model for evaluating the oil content in shales. Energy 239, 121848. https://doi.org/10.1016/j.energy.2021.121848.
Wang, F.Y., Chang, S.L., 2024. Molecular dynamics investigation of shale oil occurrence and adsorption in nanopores: unveiling wettability and influencing factors. Chem. Eng. J. 481 (1), 148380. https://doi.org/10.1016/j.cej.2023.148380.
Wang, Q., Huang, L., 2019. Molecular insight into competitive adsorption of methane and carbon dioxide in montmorillonite: effect of clay structure and water content. Fuel 239, 32–43. https://doi.org/10.1016/j.fuel.2018.10.149.
Wang, Z.J., Li, S.Y., Jin, Z.J., et al., 2023. Oil and gas pathway to net-zero: review and outlook. Energy Strategy Rev. 45, 101048. https://doi.org/10.1016/j.esr.2022.101048.
Wu, Q.Y., Wang, Y.Y., 2022. How does carbon emission price stimulate enterprises' total factor productivity? Insights from China's emission trading scheme pilots. Energy Econ. 109, 1059990. https://doi.org/10.1016/j.eneco.2022.105990.
Xia, D., Li, Q., Xue, Q.Z., et al., 2016. Super flexibility and stability of graphene nanoribbons under severe twist. Phys. Chem. Chem. Phys. 18 (27), 18406–18413. https://doi.org/10.1039/c6cp02580c.
Xue, Q.Z., Tao, Y.H., Liu, Z.L., et al., 2015. Mechanism of oil molecules transportation in nano-sized shale channel: MD simulation. RSC Adv. 5 (33), 25684–25692. https://doi.org/10.1039/c4ra16682e.
Yekeen, N., Padmanabhan, E., Abdulelah, H., et al., 2021. CO_2/brine interfacial tension and rock wettability at reservoir conditions: a critical review of previous studies and case study of black shale from Malaysian formation. J. Pet. Sci. Eng. 196, 107673. https://doi.org/10.1016/j.petrol.2020.107673.
Yoshimitsu, Z., Nakajima, A., Watanabe, T., et al., 2002. Effects of surface structure on the hydrophobicity and sliding behavior of water droplets. Langmuir 18 (15), 5818–5822. https://doi.org/10.1021/la020088p.
Yu, X.R., Li, J., Chen, Z.X., et al., 2020. Molecular dynamics computations of brine-CO_2/CH_4-shale contact angles: implications for CO_2 sequestration and enhanced gas recovery. Fuel 280, 118590. https://doi.org/10.1016/j.fuel.2020.118590.
Zendehboudi, S., Rezaei, N., Lohi, A., 2018. Applications of hybrid models in chemical, petroleum, and energy systems: a systematic review. Appl. Energy 228, 2539–2566. https://doi.org/10.1016/j.apenergy.2018.06.051.
Zhang, H.M., Thanh, H.V., Rahimi, M., et al., 2023. Improving predictions of shale wettability using advanced machine learning techniques and nature-inspired methods: implications for carbon capture utilization and storage. Sci. Total Environ. 877, 162944. https://doi.org/10.1016/j.scitotenv.2023.162944.
Zhang, Q., Liu, J., Wang, G., et al., 2024. A new optimization model for carbon capture utilization and storage (CCUS) layout based on high-resolution geological variability. Appl. Energy 363, 123065. https://doi.org/10.1016/j.apenergy.2024.123065.
Zhao, D., Liu, X.Q., Shen, Z.Y., 2023. Effect of oxygen-containing functional groups on the wettability of coal through DFT and MD simulation. Arab. J. Chem. 16 (4), 104606. https://doi.org/10.1016/j.arabjc.2023.104606.
Zhao, X., Jin, H., 2020. Correlation for self-diffusion coefficients of H_2, CH_4, CO, O_2 and CO_2 in supercritical water from molecular dynamics simulation. Appl. Therm. Eng. 171, 114941. https://doi.org/10.1016/j.applthermaleng.2020.114941.
Zhong, J., Wang, P., Zhang, Y., et al., 2013. Adsorption mechanism of oil components on water-wet mineral surface: a molecular dynamics simulation study. Energy 59, 295–300. https://doi.org/10.1016/j.energy.2013.07.016.
Zhou, J., Zhang, J.J., Yang, J.P., et al., 2022. Mechanisms for kerogen wettability transition from water-wet to CO_2-wet: implications for CO_2 sequestration. Chem. Eng. J. 428, 132020. https://doi.org/10.1016/j.cej.2021.132020.
Zhu, L., Xue, Q.Z., Li, X.F., et al., 2015. Theoretical prediction of hydrogen separation performance of two dimensional carbon network of fused pentagon. ACS Appl. Mater. Interfaces 7 (51), 28502–28507. https://doi.org/10.1021/acsami.5b09648.